agronomy

Article

Impact of Airflow Rectification on Spreading Uniformity for UAV-Based Multichannel Pneumatic Granular Fertilizer Spreader

Xunwei Wang [1,2,3,4], Rui Jiang [1,2,3,4], Zhiyan Zhou [1,2,3,4,*], Junhao Huang [1,2,3,4] and Jianqin Lin [1,2,3,4]

1 College of Engineering, South China Agricultural University/Guangdong Engineering Research Center for Agricultural Aviation Application (ERCAAA), Guangzhou 510642, China; 20201009007@stu.scau.edu.cn (X.W.); ruiojiang@scau.edu.cn (R.J.); boulete@stu.scau.edu.cn (J.H.); 602015148@stu.scau.edu.cn (J.L.)
2 Guangdong Provincial Key Laboratory for Agricultural Artificial Intelligence (GDKL-AAI), Guangzhou 510642, China
3 Key Laboratory of Key Technology on Agricultural Machine and Equipment, South China Agricultural University, Ministry of Education, Guangzhou 510642, China
4 National Center for International Collaboration Research on Precision Agricultural Aviation Pesticides Spraying Technology (NPAAC), Guangzhou 510642, China
* Correspondence: zyzhou@scau.edu.cn; Tel.: +86-13560026139

Abstract: Unmanned aerial vehicles (UAVs) are an important part of smart farms and have been widely used in granular fertilizer spreading. The multichannel pneumatic granular fertilizer spreader (MPGFS) has the advantages of light weight and precision spreading, and has been applied to UAV variable rate fertilization. Based on the problem that the airflow field disorder of the existing MPGFS reduces the uniformity of spreading, the aim of this study was to further improve the performance of the MPGFS through rectification. The computational fluid dynamics and discrete element method (CFD-DEM) and coupling simulation method were used to study the characteristics of the airflow field and fertilizer particle motion, and a honeycomb rectifier and grid rectifier were developed. The aperture of the honeycomb rectifier and the grid size of the grid rectifier were optimized. Then, the test bench was built to test the consistency of the discharge rate of each channel and the spreading uniformity of the MPGFS. The simulation results of the existing MPGFS showed that the airflow provided by the axial flow fan was rotational, and this caused the particles' motion to be skewed in the shrinkage section, so the discharge rate of each channel was inconsistent. The airflow field analysis results of the shrinkage section showed that the airflow rotation was reduced after the rectification of the honeycomb rectifier and the grid rectifier. The bench test results showed that the coefficient of variation (CV) of each channel discharge rate of the existing MPGFS was 20.16%, the optimal honeycomb rectifier was 13.07%, and the optimal grid rectifier was 5.27%. The bench test results of spreading uniformity show that the CV of spreading uniformity of the existing MPGFS was 15.32%, the optimal honeycomb rectifier was 15.81%, and the optimal grid rectifier was 8.02%. The grid rectifier spread pattern was more reasonable and the CV of uniformity was better. This study demonstrated that the use of a grid rectifier to rectify the airflow field of MPGFS can effectively improve its spreading uniformity, which was of guiding significance for the design and research of MPGFS.

Keywords: UAV; pneumatic; grid rectifier; honeycomb; spreader

Citation: Wang, X.; Jiang, R.; Zhou, Z.; Huang, J.; Lin, J. Impact of Airflow Rectification on Spreading Uniformity for UAV-Based Multichannel Pneumatic Granular Fertilizer Spreader. *Agronomy* **2023**, *13*, 2661. https://doi.org/10.3390/agronomy13102661

Academic Editor: Xiongkui He

Received: 30 August 2023
Revised: 9 October 2023
Accepted: 11 October 2023
Published: 23 October 2023

1. Introduction

Unmanned aerial vehicles (UAVs) have become an important part of the smart farm, and are mainly used in remote sensing monitoring [1], liquid spraying [2,3], seeding [4], harvesting [5,6], spreading and other fields [7]. In particular, paddies are difficult to access for fertilization using large-scale ground machinery in small fields of hilly mountainous areas and deep mud fields. Because the UAV has the characteristics of small size, no runway and automatic obstacle avoidance, it has unique advantages for operation in these areas [8].

Currently, the spreaders are generally developed to spread granular material on UAVs. Li et al. designed a rice seed spreader suitable for UAVs. The device was designed as a reverse-pyramid-shaped seed hopper for matching the UAV [9]. The rice seeds fall into the disc spreader due to gravity, and an electric gate is designed to control the start and stop of the spreader. The feasibility of using UAVs to sow rice was verified through field experiments. In order to improve the uniformity of the rice seed spreading of the disc spreader, Wu et al. designed a disc spreader with a baffle ring, and optimized it using the discrete element method (DEM) [10]. Gao et al. developed a spreader combining a screw conveyer and disc for green manure seeds, which can control the discharge rate more accurately [11]. Ren et al. improved the disc spreader for the application of rice topdressing fertilizer, A gate-type discharge device was designed to control the amount of fertilizer [12].

A variable rate of fertilization is an important field management technology that has the effect of saving fertilizer, increasing economic and environmental benefits in smart farms [13,14]. It requires an accurate fertilization amount and fertilization position. The disc spreader usually uses a gate to control the amount of fertilizer, so that the amount of fertilizer is not accurately controlled. At the same time, it is spread to the surrounding area with a large spread range, so that the fertilization position is not accurate [15]. In view of these deficiencies of the disc spreader, Song et al. designed a multichannel pneumatic granular fertilizer spreader (MPGFS) suitable for UAV by referring to the spreader of large manned aircraft [16]. MPGFS can control the amount of fertilizer with high precision by using groove wheel discharge device, and the distribution of spreading is more accurate for banding spreading [17,18].

UAVs are different from manned aircrafts in that they fly at a low speed and the MPGFS cannot obtain ram-air from the forward velocity of the aircraft. They need a ducted fan to supply airflow for MPGFS. However, the airflow supplied by the axial flow fan is a disorderly airflow field, and this may cause the uneven discharge rate of each channel, thereby affecting the uniformity of fertilizer spreading. CFD-DEM is an important means to study the gas–solid two-phase flow, especially to study the motion of discrete particles and the effect of the airflow on particles. Gao et al. used the CFD-DEM method to simulate the particle motion characteristics in the quantitative seed feeding system [19]. Lei et al. simulated the seed feeding device of a Venturi structure based on the CFD-DEM method [20]. Li et al. simulated the pneumatic conveying seeding system by using the CFD-DEM method, and realized the prediction of seed-conveying velocity [21].

The aim of this work was to design a UAV-based MPGFS suitable for variable rate fertilization, and to improve the performance of the MPGFS by rectifying the airflow field. The computational fluid dynamics and discrete element method (CFD-DEM) coupling simulation methods were used to analyze the characteristics of the airflow field and the mechanism of the airflow field on the fertilizer particles. Rectifiers were developed and optimized using airflow field analysis and bench test. Finally, the performance of the optimized spreader was tested using an indoor static spreading test.

2. Materials and Methods

2.1. The Variable Fertilization UAV

The variable rate fertilization UAV was self-assembled, and was mainly composed of six-rotor UAV frame, power system, flight control system, ground control station, and spreading system (Figure 1). The UAV frame was produced by EFT Electronic Technology Co., Ltd., Hefei China. The flight control system was DJI A3 provided by DJI Innovation Technology Co., Ltd., Shenzhen China. The ground control station was a self-developed app based on Android mobile phone. The spreading system consisted of a fertilizer box, a MPGFS, a spreading controller, a spreader power supply module, and an infrared residual material monitoring module. The UAV had a load of 30 kg and a no-load endurance time of about 18 min. It could carry out route planning, autonomous operation and breakpoint continuing operation.

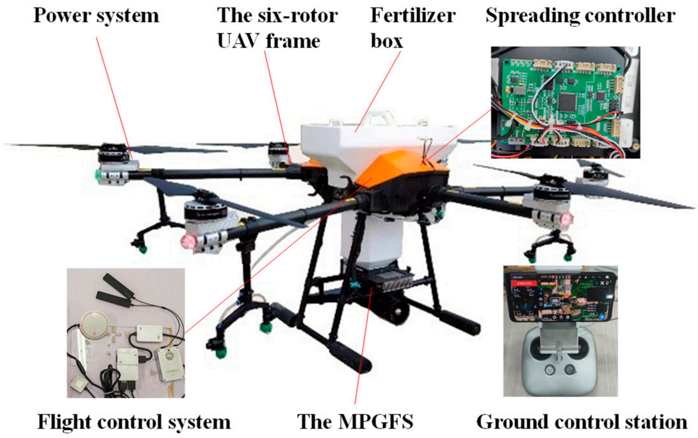

Figure 1. The structure of variable fertilization unmanned aerial vehicle (UAV).

After the crop growth information was obtained using the multi-spectral remote sensing UAV, the fertilization prescription map was generated according to the fertilization decision model [22]. The fertilization prescription map was a Geojson format file that divides the fertilization plot into 10 m × 10 m grids and records the geographic coordinates and fertilization amount information. The fertilization prescription map was imported into the app, and the rotation speed of the groove wheel was calculated by combining the position coordinates, flight speed and spreading width of the UAV. Then, the rotation speed of the groove wheel command was sent from the ground control station to the spreading controller, and the rotation speed of the groove wheel was adjusted to realize variable fertilization.

2.2. Structure and Working Principle of the MPGFS

The MPGFS consisted of a discharge device and a pneumatic spreader with multichannel, as shown Figure 2. The fertilizer discharged by the discharge device falls into the shrinkage section of the pneumatic spreader, and the high-speed airflow from the shrinkage section blows the fertilizer to the rear of the UAV. The multichannel of the spreader was used to diffuse the fertilizer.

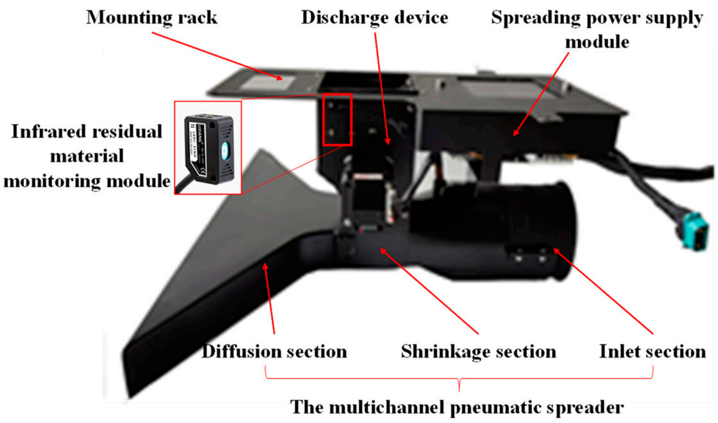

Figure 2. The structure of multichannel pneumatic granular fertilizer spreader (MPGFS).

2.2.1. The Discharge Device

The groove wheel fertilizer discharger device is widely used in ground variable fertilization machinery, which had the advantages of simple structure, high reliability and precise fertilization amount [23,24]. In this work, the rotating upper groove wheel discharge device was designed to ensure accurate fertilization, as shown Figure 3. The discharge device was designed with an offset of clearing fertilizer plate to prevent fertilizer leakage and an anticlogging gap to prevent blockage. The grooved wheels with six grooves and six staggered columns were designed to reduce the pulsation of the discharge rate [25], as shown Figure 4.

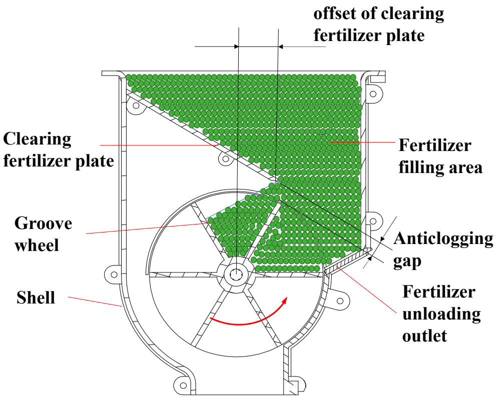

Figure 3. The structure diagram of discharge device.

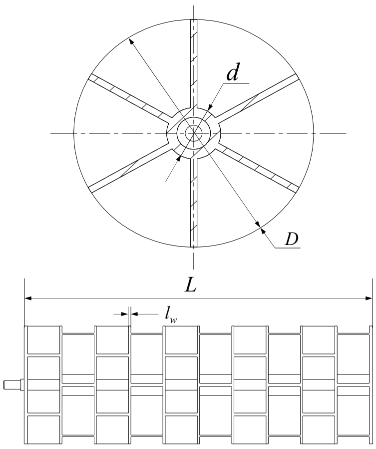

Figure 4. The structure diagram of groove wheel.

The discharge rate formula of the groove wheel discharge device was established.

$$Q = N_g(Q_1 + Q_2) \tag{1}$$

$$Q_1 = \rho_v z_r (L - z_a l_w) f_z \varphi \tag{2}$$

$$Q_2 = \rho_v \pi D L \tau_d \tag{3}$$

$$f_z = \frac{\pi}{z_r}\left(\left(\frac{D}{2}\right)^2 - \left(\frac{d}{2}\right)^2\right) \tag{4}$$

where Q is the discharge rate (kg/min), Q_1 is the amount of one-circle fertilizer in the groove (kg/r); Q_2 is the amount of one-circle fertilizer in the driving layer (kg/r); N_g is the rotational speed of the groove wheel (rpm); ρ_v is the fertilizer volume density (kg/m^3); Z_r is the groove number; L is the length of groove wheel (m); Z_a is the column's number of grooves; l_w is the thickness of grooved wheel ribs (m); f_z is the cross-sectional area of a single groove (m^2); φ is the fullness coefficient of the fertilizer in the groove; D is the diameter of the groove wheel (m); d is the diameter of groove wheel axle (m); and τ_d is the characteristic parameter of the driving layer.

According to the discharge rate formula, there was a linear relationship between the rotational speed of the groove wheel and the discharge rate. The rotational speed of the groove wheel was used as the adjustment parameter of the discharge rate applied in the variable rate fertilization, which was adjusted by the stepping motor. The length and diameter of the groove wheel were designed according to the Formulas (1)–(4). The length was 100 mm, and the diameter was 60 mm.

2.2.2. The Multichannel Pneumatic Spreader

The multichannel pneumatic spreader was composed of three parts: inlet section, shrinkage section and diffusion section, as shown Figure 2. The axial flow ducted fan had the characteristics of high speed, light weight and large air volume rate, and was applied to the jet aircraft model. In this work, the inlet airflow was provided by the 90 mm diameter ducted fan. The start–stop and speed of the ducted fan can be controlled through electric adjustment. After testing, the ducted fan speed was set to 18,000 rpm; the airflow velocity was feasible for successfully spreading and enough width. The cross-sectional area of the shrinkage section was a rectangle with the width of the groove wheel and 30 mm thickness. The cross-sectional area of the shrinkage section decreases, the airflow velocity increases, and the pressure decreases. There was a fertilizer inlet above the shrinkage section, and with the negative pressure generated by the Venturi principle, this made the fertilizer smoothly flow into the airflow and mix. In the diffusion section, the mixed flow of gas and fertilizer was divided into multiple channels and spread to different angles in the rear.

The airflow provided by the axial flow ducted fan was still rotational, although it has a guide plate. In order to eliminate the rotation of the airflow, honeycomb rectifiers and grid rectifiers had been developed, and their installation positions are shown in Figure 5. To make the structure compact, the thickness of the honeycomb was 20 mm, and different apertures of 5–20 mm were designed for research. The honeycomb rectifier was installed behind the ducted fan. The grid rectifier was a truncated pyramid type with an internal grid divided into n rows and m columns, and the model was named $n \times$ m. The grid rectifier was installed at the inlet of the shrinkage section.

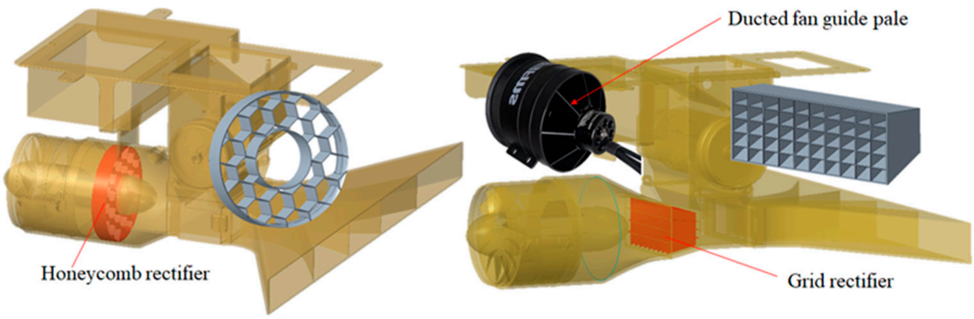

Figure 5. The structure and installation method of honeycomb rectifier and grid rectifier.

2.3. Simulation Methods

2.3.1. Mathematical Model

In this work, CFD-DEM was used to analyze the airflow field and to track the trajectory of fertilizer particles. When particle moved in the airflow, particle was subjected to contact force with particles or wall (F_{ij}), particle–fluid interaction force (F_{f-p}) and gravity ($m_i g$). The motion of particles follows Newton's second law, which is governed by the force balance equation.

$$m_i \frac{dv_i}{dt} = F_{f-p} + \sum_{j=1}^{k_i+k_w} F_{ij} + m_i g \quad (5)$$

$$I_i \frac{d\omega_i}{dt} = \sum_{j=1}^{k_i+k_w} T_{ij} + T_{f-p} \quad (6)$$

where m_i, v_i and ω_i are the mass, velocity and angular velocity of particle i; F_{f-p} is the fluid–particle interaction force; F_{ij} is the contact force between particle i with particle or wall j; $m_i g$ is gravity of particle i; T_{ij} is the torque between particle i and particle or wall j, and T_{f-p} is the torque of fluid–particle interaction.

The contact force between the particles F_{ij} was solved by the Hertz–Mindlin (no slip) model and the standard rolling friction model. The detailed mathematical model has been introduced [26,27].

It has been verified that in addition to the drag and Saffman lift between the airflow and the fertilizer particles, the Magnus force must also be considered in calculation [28], which is as follows.

$$F_{f-p} = F_d + F_s + F_m \tag{7}$$

where F_d is the drag force, F_s is the Saffman lift force, and F_m is the Magnus lift force.

The drag force on fertilizer particle was calculated from the following equation:

$$F_d = 0.5 C_D \rho_f A_p (v_f - v_p) \left| v_f - v_p \right| \tag{8}$$

where ρ_f is the gas density; A_p is the projected area of the particle, v_f is the velocity of gas, v_p is the velocity of particle, and C_D is the drag coefficient, calculated as given [29].

$$C_D = \begin{cases} \dfrac{24}{Re} & Re \le 0.5 \\ \dfrac{24(1 + 0.15 Re^{0.687})}{Re} & 0.5 \le Re \le 1000 \\ 0.44 & Re \ge 1000 \end{cases} \tag{9}$$

$$Re = \frac{\delta \rho_f d_p \left| \vec{v}_f - \vec{v}_p \right|}{\mu} \tag{10}$$

where Re is the Reynolds number, d_p is the diameter of the particle, μ is the fluid viscosity, δ is the porosity of the CFD computational cell.

The Saffman lift force exerted on particle is given by

$$F_s = 1.61 d_p^2 \sqrt{\mu \rho_f} (v_f - v_p) \times \frac{\nabla \times v_f}{\sqrt{\left| \nabla \times v_f \right|}} \tag{11}$$

The Magnus lift force embodies relative motion between particle and fluid. It is expressed by the following:

$$F_m = \frac{1}{8} \pi d_p^3 \rho_f \frac{Re_p}{Re_r} C_m \left[\left(\frac{1}{2} \nabla \times \vec{v}_f - \vec{\omega}_p \right) \times \left(\vec{v}_f - \vec{v}_p \right) \right] \tag{12}$$

$$\begin{cases} Re_r = \rho_f d_p^2 \left| \frac{1}{2} \nabla \times \vec{v}_f - \vec{\omega}_p \right| / \mu \\ Re_p = \left| v_f - v_p \right| d_p / \mu \\ C_m = 0.45 + \left(\dfrac{Re_r}{Re_p} - 0.45 \right) e^{-0.05684 Re_r^{0.4} Re_p^{0.3}} \end{cases} \tag{13}$$

where ω_p is the angular velocity of particle.

The gas phase flow was delivered from ducted fan to diversion outlet. The gas phase, which was treated as a continuous phase, strictly follows the mass conservation law and momentum conservation law. The detailed mathematical model has been introduced [30]. In this study, the one-way coupling method was used, and the DEM information was not transmitted back to the CFD model, ignoring the influence of particles on the airflow field.

2.3.2. Simulation Conditions

The model of the multichannel pneumatic spreader was reasonably simplified, and the airflow domain was extracted for meshing. The tetrahedral CFD cells were meshed using the meshing module of ANSYS 2019.0 software (ANSYS, Inc., Canonsburg, PA, USA), The total number of meshes was 473,501. The Fluent module was used to solve the airflow field. The multiple rotating reference frame (MRF) method was applied to couple the rotating blade of ducted fan and stationary casing [31,32]. In the simulation, the ducted fan speed was set to 18,000 rpm, which was close to the measured value. The feasibility of applying the realizable $k - \varepsilon$ turbulence model to solve a rotating flow and mixing flow have been verified, and good agreement between simulated and experiment results has been found [32,33]. The SIMPLE algorithm solved the coupling of the velocity and the pressure field, which promotes convergence in the computation of complex flows. The air inlet of the ducted fan in pressure inlet was established to have a value of 0 Pa. The outlets of the five channels and the fertilizer inlet in the shrinkage section constituted the pressure outlet, which had a value of 0 Pa. Walls were assumed to be made of aluminum and their positions were fixed.

The solid particle phase was solved in EDEM 2022. Compound fertilizer (Henan Xinlianxin Chemicals Group Co., Ltd., Xinxiang, China) was selected as the sample, its shape was approximately spherical, and the its particle diameter was normal distribution. The average particle diameter was 2.96 mm, and the standard deviation was 0.28. The single sphere model was chosen as particle model. It has been found that the Hertz–Mindlin (no-slip) model and the standard rolling friction model can accurately solve the force between fertilizer particles [34–36]. The static friction coefficient between particles and models was measured using tilt method. The static friction coefficient and rolling friction coefficient between particles were calibrated using the stacking angle of fertilizer particles (detailed test methods and other parameters in reference [37] and listed in Table 1). A particle production rate of 5 kg/min occurred in fertilizer inlet of shrinkage section. After the CFD simulation calculation was completed, the airflow field results were exported and imported into the EDEM 2022 software. According to the above mathematical model, the force of particles was calculated, in which the force of airflow on particles was applied in the form of particle body force.

Table 1. DEM simulation parameter settings [37].

Parameters	Particles	Models
Poisson's ratio	0.24	0.47
Shear modulus/Pa	3.4×10^7	2×10^6
Solid density/kg·m^{-3}	1155	1060
Coefficient of restitution with particles	0.27	0.50
Coefficient of rolling friction with particles	0.26	0.71
Coefficient of static friction with particles	0.03	0.05

2.4. Bench Test and Evaluation Index

2.4.1. Discharge Rate Consistency Test of Each Channel

The guide plates in the diffusion section were designed to be equally spaced, and the fertilizer would be equally divided into each channel under ideal conditions. The equal discharge rate of each channel was the basis for the design of the diffusion section. The discharge rate consistency of each channel of the MPGFS directly affects the uniformity of the fertilizer spreading. Hence, the discharge rate of each channel of the MPGFS was conducted. Moreover, compared with the simulation results, the reliability of the simulation model was verified.

The tests were assigned three groups: control group, honeycomb rectifiers, and grid rectifiers. As in the simulation design, there were four level tests in honeycomb group and grid rectifier group to optimize the parameters. During the test, the rotational speed of the grooved wheel was 30 rpm, and the rotational speed of the ducted fan was approximately

18,000 rpm. The fertilizer was collected at each outlet with a net bag. At the end of each test, the net bag was removed, and the quality of the fertilizer in each net bag was weighed using an electronic scale. The layout of the test bench was shown in Figure 6.

Figure 6. Test benches for the discharge rate consistency of each channel.

To reduce the test error, all of the tests were repeated three times, and the average value was taken. For the tests, coefficient of variation (CV) was applied to evaluate the consistency of each channel discharge rate. Its calculation equation was as follows:

$$\overline{x_j} = \frac{1}{n}\sum_{i=1}^{n} x_{ij} \tag{14}$$

$$\overline{x} = \frac{1}{k}\sum_{j=1}^{k} \overline{x_j} \tag{15}$$

$$p_j = \frac{\overline{x_j}}{\overline{x}} \times 100\% \tag{16}$$

$$\sigma = \sqrt{\frac{1}{k-1}\sum_{j=1}^{k} (\overline{p_j} - \overline{p})^2} \tag{17}$$

$$C_v = \frac{\sigma}{\overline{x}} \times 100\% \tag{18}$$

where $\overline{x_j}$ is the average discharge rate of the channel j of the MPGFS, g/min; x_{ij} is the discharge rate of the channel j of the MPGFS in the i-th test, g/min; $\overline{x}$ is the average value of the discharge rate of each channel of the MPGFS, g/min; n is the number of tests; k is the number of channels of the MPGFS; p_j is the percentage of the discharge rate of the j number (PDR-j) of the channel of the MPGFS; σ is the standard deviation of the discharge rate of each channel of the MPGFS; and C_v is the CV of the discharge rate of each channel of the MPGFS.

2.4.2. Test Method of the Spreading Uniformity of the MPGFS

The fertilizer spreading uniformity of the rectified MPGFS was tested at the South China Agricultural University. The indoor operation could avoid the interference of natural wind and UAV rotor wind, which was helpful to analyze the influence of the MPGFS on the spreading uniformity. The static two-dimensional spread pattern can be obtained using indoor static test, which was of great significance for analyzing the MPGFS mechanism and optimization of the MPGFS.

In the test, the MPGFS and fertilizer box were placed on the elevator, which rose to 5 m above the ground from the MPGFS outlet. The MPGFS was in a static state and did not rise under the UAV, and was controlled by a ground computer. A total of 512 collector cartons, each with dimensions of 400 by 400 mm wide and 100 mm deep, were used to cover the spreading area of 81.92 m^2, as shown Figure 7.

Figure 7. The indoor static spreading test bench.

Single factor test was carried out with different rectifier types as factors and no rectifier as control group. The ducted fan rotational speed was approximately 18,000 rpm. The grooved wheel rotational speed was 30 rpm. The spreading fertilizer amount was about 1.5 kg. The weight of fertilizer in each collector carton was measured to directly determine the static spread pattern using an electronic scale with an accuracy of 0.01 g.

Based on static spread pattern, the simulation moving spread pattern was derived to analyze the spreading uniformity and width through the following steps [38]. (1) The sum of fertilizer amount collected in each column along the simulated moving direction of the MPGFS was divided by the total amount of fertilizer to normalize, and the moving one-dimensional spread pattern was obtained. (2) The CV of uniformity under different widths was calculated by using method of simulated overlay route [39]. (3) The simulation moving spread pattern was obtained by using minimum CV as the optimal width. Note that the CV was not the actual spreading uniformity in the field, and the results were only used for evaluation of static spreading uniformity. Without the interference of other factors such as natural wind, the uniformity was often better.

3. Results and Discussions

3.1. Validation Simulation Model

The MPGFS without rectifier was simulated. The total mass of particles entering each channel was counted, respectively. The percentage of each channel discharge rate calculated according to Formula (16) was compared with the bench test results, as shown in Table 2 and Figure 8. Note that the difference in the spreading time of the simulation and the bench test leads to a large difference in the fertilizer quantity, so the percentage of the discharge rate of each channel was used for comparison. The results showed that the maximum error was −10.62%, and the minimum error was 1.40%. The distribution trends of the percentage of the discharge rate of each channel were similar.

Table 2. The percentage of the discharge rate of each channel.

Items	Channel 1	Channel 2	Channel 3	Channel 4	Channel 5
Simulation value	17.71%	25.52%	17.71%	15.63%	23.44%
Bench test value	16.84%	23.58%	17.46%	15.89%	26.22%
Error rate	5.15%	8.22%	1.40%	−1.68%	−10.62%

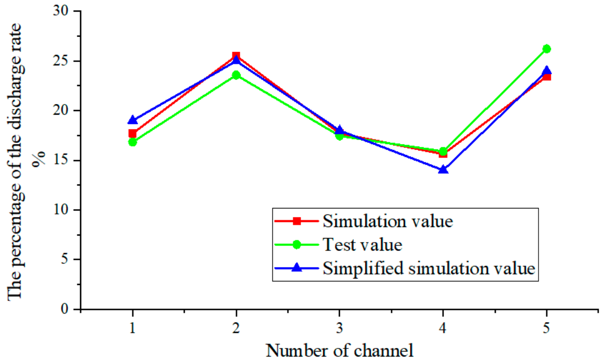

Figure 8. Comparison of the percentage of the discharge rate of each channel between simulation and test.

3.2. Airflow Field Characteristics of MPGFS

The airflow field velocity contour of the MPGFS without the rectifier is shown in Figure 9. It can be observed that the airflow velocity increases with the decrease in the cross section during the transition from the outlet of the fan to the shrinkage section. At the diffusion section, the airflow was shunted to each channel, and the airflow velocity was gradually reduced. The shrinkage section was the key section where the fertilizer particles were accelerated and distributed to each channel, which needed to be focused on. Due to the change in cross section shape, the airflow field in the shrinkage section was non-uniform. The airflow velocity on both sides was greater than that in the middle. In the shrinkage section, the average airflow velocity was 35.18 m/s.

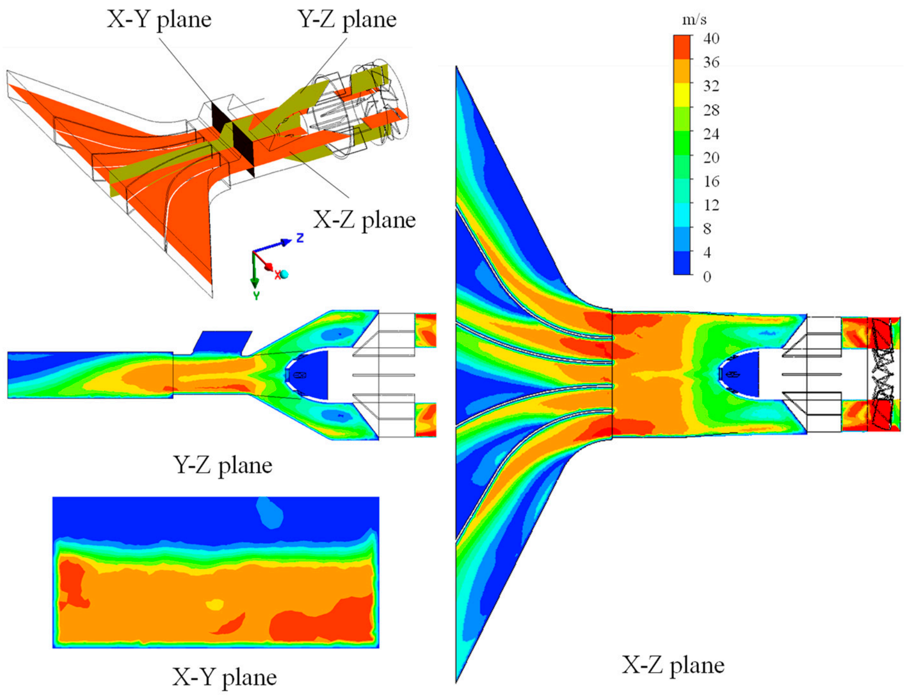

Figure 9. The airflow field velocity contour of MPGFS without rectifier.

The velocity vector of the airflow in the plane can show the direction of airflow movement. The tangential velocity vector of the airflow field in the X-Y plane of the shrinkage section is shown in Figure 10. It can be clearly observed that there were three rotation centers, which were clockwise rotation, inverse rotation and clockwise rotation from left to right. It can be assumed that the inconsistency of the displacement of each channel was caused by the rotation of the airflow field, and the following particle trajectory analysis also confirms this assumption. There were two reasons for the multiple vortices in the airflow field: 1. The airflow at the outlet of the ducted fan was rotational, and 2. the cross section was changed during the transition from the outlet of the ducted fan to the shrinkage section, and the change in the cross section led to the occurrence of vortices.

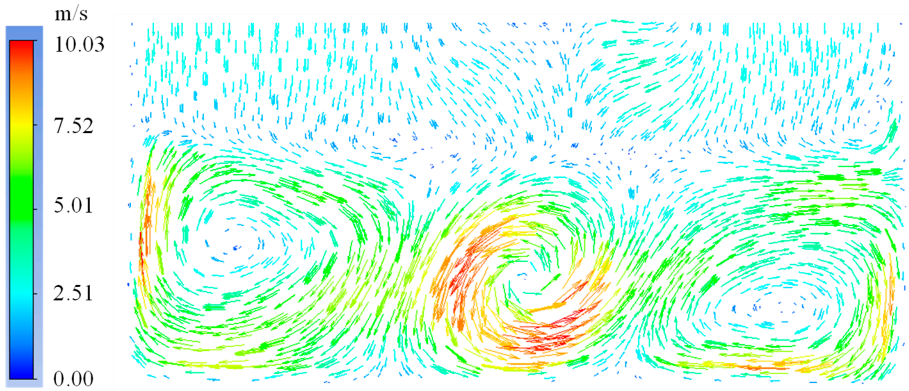

Figure 10. The tangential velocity of the airflow field in the shrinkage section of MPGFS without rectifier.

3.3. The Motion Characteristics of Particles in the Shrinkage Section

In order to observe the trajectory of fertilizer particles more clearly, the number of simulated particles was reduced. A total of 100 fertilizer particles with the same diameter were uniformly generated in the width direction of the fertilizer inlet. The number of particles entering each channel was counted and compared with the test results, as shown Figure 8. The simplified simulation results show that it still had the distribution characteristics of each channel discharge rate, so the simplified analysis was reasonable.

The simulation results of the fertilizer particle trajectory are shown in Figure 11. Observing the particle trajectory, it was found that there was an angle between the movement direction of most particles and the Z direction. The movement direction of the particles corresponding to channel 1 and channel 3 was skewed to channel 2, and the movement direction of the particles corresponding to channel 4 was skewed to channel 5.

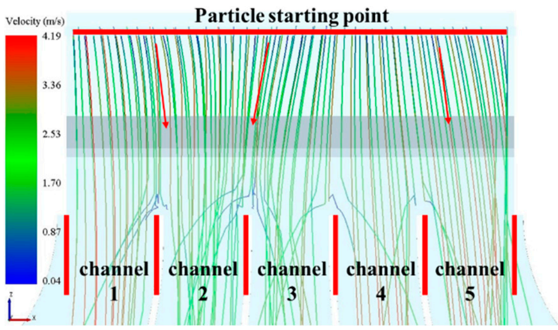

Figure 11. Fertilizer particle trajectory in the shrinkage section.

Combined with the airflow field (Figure 10), the airflow corresponding to channel 1 rotated clockwise. The airflow corresponding to channel 2 moved downward. The airflow corresponding to channel 3 rotated counterclockwise. Particles fell into the shrinkage section from the material inlet, and some particles in the corresponding positions of channels 1 and 3 moved laterally to channel 2 under the action of the tangential velocity of the airflow. This caused an increase in the number of particles in channel 2. In addition, there was an upward tangential velocity of the airflow in channel 4 that prevented particles from falling into channel 4, and some particles were laterally distributed to channels 3 and 5, resulting in a decrease in particles in channel 4.

3.4. The Influence of Honeycomb Rectifier Aperture on Airflow Field

Fertilizer particles mixed with airflow in the shrinkage section. Fertilizer particles were mainly accelerated by drag force. The rotation of the airflow made the drag force also have a component in the X-Y plane, and the magnitude of the drag force component was determined by the tangential velocity of the airflow velocity in the X-Y plane. Therefore, in this work, the tangential velocity of the airflow in the X-Y plane was used to evaluate the rectification effect of the rectifier.

The tangential velocity distribution of the airflow in the shrinkage section is shown in Figure 12, with the honeycomb rectifier. When the aperture was 5 mm and 10 mm, there was a vortex in the middle of the shrinkage section, and some airflow moved from the middle to both sides. When the aperture was increased to 20 mm, the vortex in the middle disappeared, and a vortex appeared on both sides. When the aperture was 15 mm, it was the transition state from a vortex in the middle to a vortex on both sides, with three unobvious vortexes, and the overall tangential velocity was small. When the aperture was 15 mm, the maximum tangential velocity of the shrinkage section was 4.73 m/s, which was greatly reduced compared to 10.03 m/s without honeycomb.

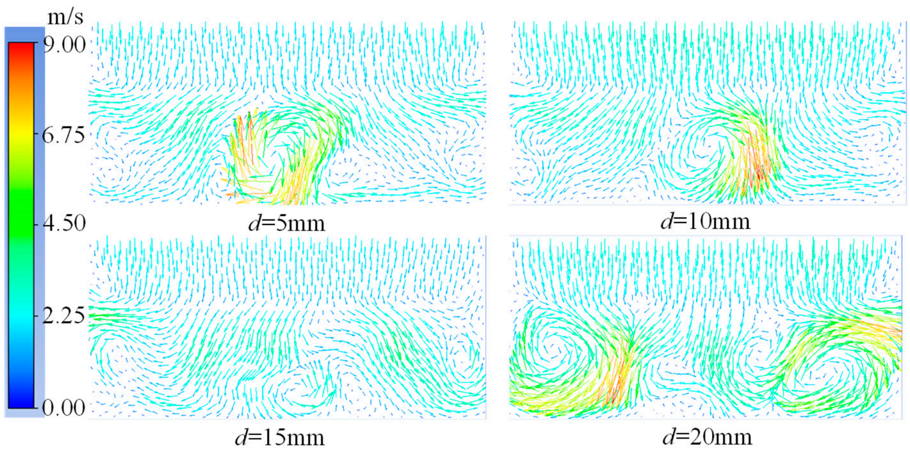

d—outer diameter of honeycomb hole.

Figure 12. The tangential velocity distribution of airflow in shrinkage section with honeycombs.

It can be seen that the design of honeycomb rectifier at the outlet of the ducted fan can reduce the tangential velocity of the shrinkage section airflow and reduce the rotation of airflow. In addition, it did not mean that the smaller honeycomb aperture had a better rectification effect. However, the airflow goes through the transition section from the circular section to the rectangular section after passing through the honeycomb. Turbulence still occurs in the shrinkage section due to uneven velocity and cross section variations.

3.5. The Influence of Grid Rectifier Size on Airflow Field

In order to design a suitable grid size, the simulation test of four grid rectifiers with different grid numbers was conducted. The distribution of tangential velocity in the shrinkage section is shown in Figure 13. The maximum tangential velocity of grid rectifier 3×6 was 5.54 m/s, and the airflow was divided into several small vortexes. The maximum tangential velocity of the grid rectifier 6×12 was 2.5 m/s. The tangential velocity of the shrinkage section decreased as the number of grid squares increased. However, the maximum tangential velocity of grid rectifier 5×10 was reduced to 2.52 m/s, and the continuous subdivision of the grid had little effect on reducing the tangential velocity. Due to the wall thickness limit of the grid rectifier, the subdivision grid led to the decrease in the outlet air velocity. When the grid was divided into 5×10, the tangential velocity of the shrinkage section was small, the main direction was downward and there was no obvious vortex. After comprehensive consideration, 5×10 was selected as the grid size.

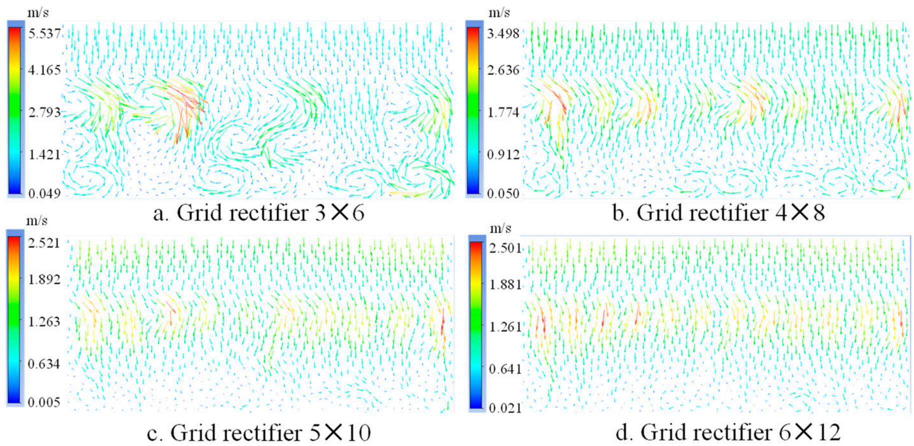

Figure 13. The tangential velocity distribution of airflow in shrinkage section with grid rectifiers.

3.6. The Consistency of Each Channel Discharge Rate

The MPGFS without the rectifier was the control group, and the honeycomb rectifiers and the grid rectifiers were the treated groups. Moreover, to reflect the airflow field analysis of the rectifier, the honeycomb rectifiers and the grid rectifiers were manufactured using 3D printing technology, and had the same structural parameters as the simulation. Each group of tests was repeated three times, and the standard deviation of each channel discharge rate of the three tests was calculated. The maximum standard deviation of each test group was 0.0448. This showed that the test repeatability was good and the data were reliable.

The results are shown in Figure 14. Channel 2 of the control group had the largest discharge rate, with a PDR-2 of 25.52%, and Channel 4 had the smallest discharge rate, with a PDR-4 of 15.63%. The CV of the discharge rate consistency of each channel was 21.20%. Combined with the results of the simulation, it was evident that the tangential velocity of the airflow in the shrinkage section was the primary factor that caused the particles to move laterally in the shrinkage section.

The CV of discharge rate consistency of each channel of the MPGFS with honeycomb was between 13.07% and 15.23%. The discharge rate of each channel shows the distribution of less discharge in the middle and more at the sides, which corresponded to the tangential airflow field distribution in the shrinkage section moving from the middle to both sides. Among the honeycombs with different apertures, the honeycomb with a 15 mm aperture was the best, and the CV of the discharge rate consistency of each channel was 13.07%. The shrinkage section airflow velocity of the pneumatic conveying system with honeycomb of different apertures was measured. The smaller the aperture, the smaller the airflow velocity in the shrinkage section. We chose the honeycomb with the aperture of 15 mm as the optimal scheme. Compared with no honeycomb, the pneumatic conveying system with honeycomb demonstrated a remarkable effect on improving the consistency of each channel discharge rate.

The CV of the discharge rate consistency of each channel of the MPGFS with a grid rectifier was between 5.03% and 7.34%. The discharge rate distribution of each model of grid rectifier was similar, and the discharge rate of channel 1 was the smallest. The test results of different models of grid rectifiers showed that with the grid subdivision, the CV of the consistency of each channel discharge rate decreased. Similarly, the measurement results of the shrinkage section airflow velocity showed that with the grid subdivision, the airflow velocity in the shrinkage section decreased. When the grid was divided into 6×12, the consistency of each channel discharge rate was the best, and the CV was 5.03%. When the grid was divided into 5×10, the CV was 5.27%, which was slightly different from the grid divided into 6×12. In summary, we chose grid 5×10 as the optimal scheme. Comparing the two optimization methods of partitions and honeycombs, the optimization effect of grid rectifiers was the best.

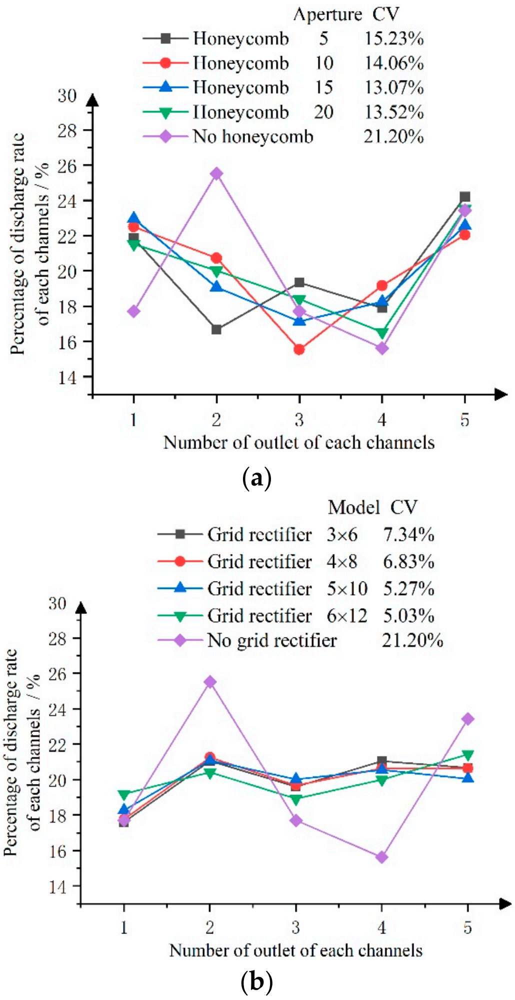

Figure 14. Discharge rate of each channel under the different partitions. (**a**) Honeycomb rectifier group. (**b**) Grid rectifier group.

3.7. The Spreading Uniformity

The static spread patterns of the control group and the optimized MPGFS is shown in Figure 15. For the control group, the honeycomb aperture was 15 mm, the grid rectifier model was 5 × 10. The results of the control group without the rectifier showed maximum deposition on the left side, with a peak of 12.90 g. At the peak, fertilizer and airflow velocity were more uneven, resulting in a closer blowing distance. The spread patterns of the honeycomb and grid rectifier were circular arcs, and there was no obvious peak. The asymmetry occurs at both ends, and the deposition at the left end was less than that at the right end. The grid rectifiers were better spread patterns than honeycombs.

Figure 16 showed the simulation moving spread patterns of control group and optimized MPGFS. The results of the control group showed that the minimum uniformity CV was 15.32%, and the available width was 8 m. The minimum uniformity CV was 15.81% and the available width was 8.8 m for the MPGFS with a honeycomb rectifier. The minimum uniformity CV was 8.02% and available width was 8.4 m for the MPGFS with a grid rectifier. There was no simulated superposition route from the point of view of moving one-dimensional spread pattern; there were single peaks in the control group. Both the honeycomb rectifier and grid rectifier had no obvious peaks, and were more distributed on the right side. The asymmetry of both sides of the static spread pattern affects the uniformity of the moving spread pattern of the simulated superposition route. The excessive discharge rate of channel 5 on the right side leads to the poor symmetry of the deposition distribution in the honeycomb rectifier group, resulting in poor uniformity. Regardless of the static spread patterns and the simulated moving spread patterns, the comparison of each optimization scheme showed that the grid rectification result was better.

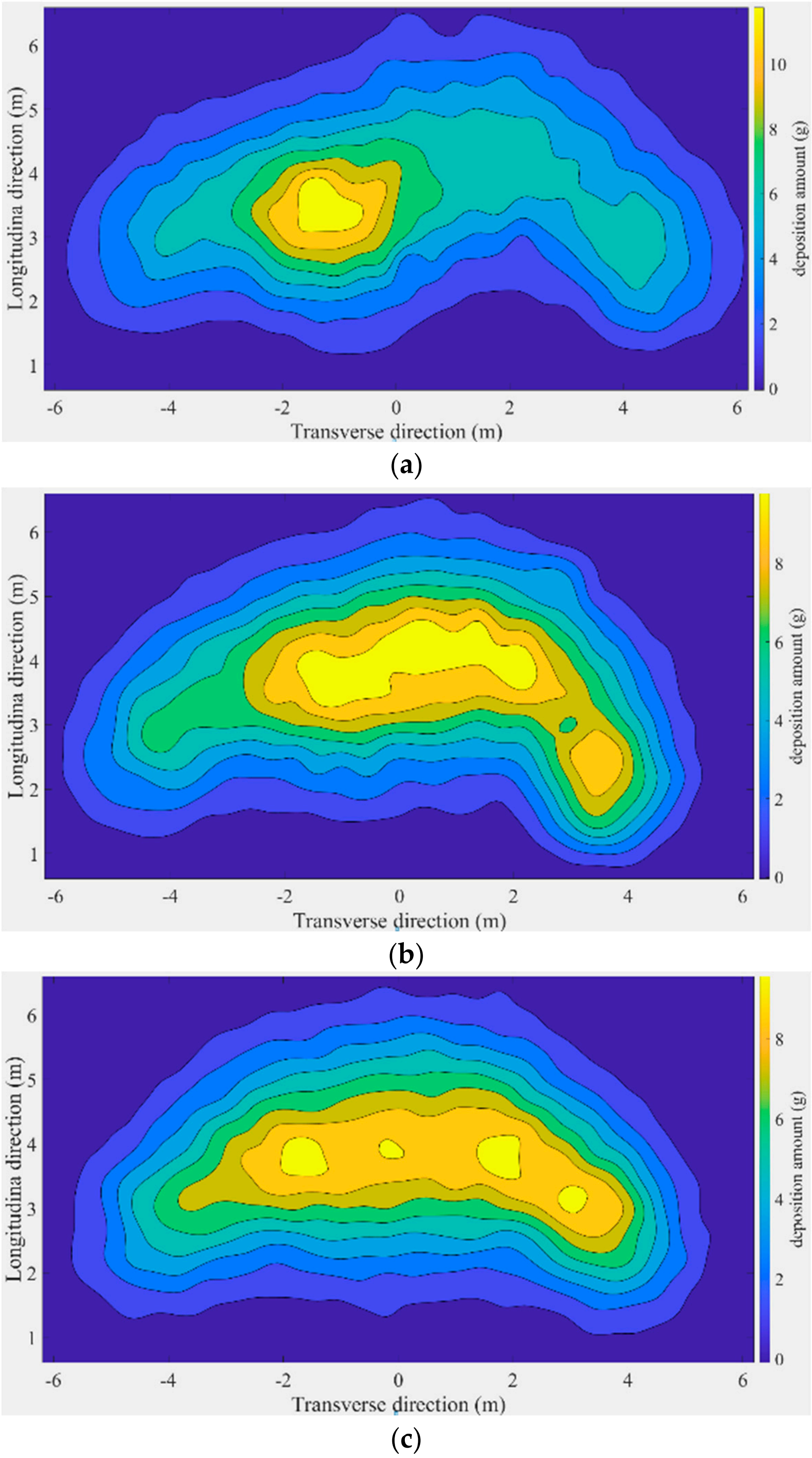

Figure 15. Static spread patterns. (**a**) Control group. (**b**) Honeycomb rectifier. (**c**) Grid rectifier.

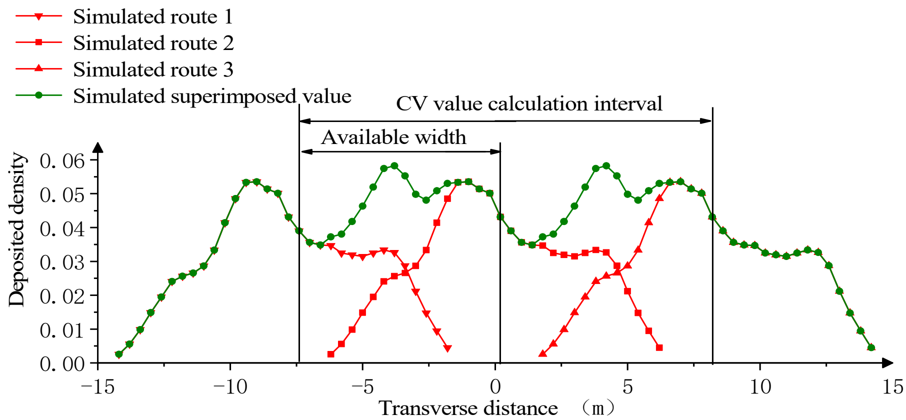

(**a**)

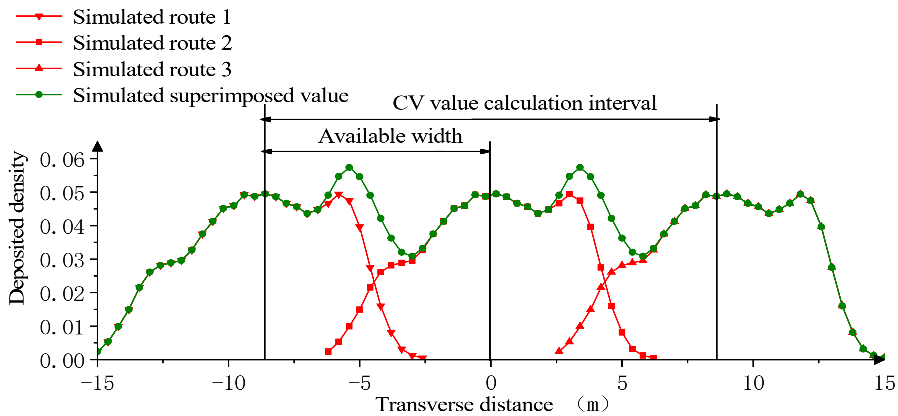

(**b**)

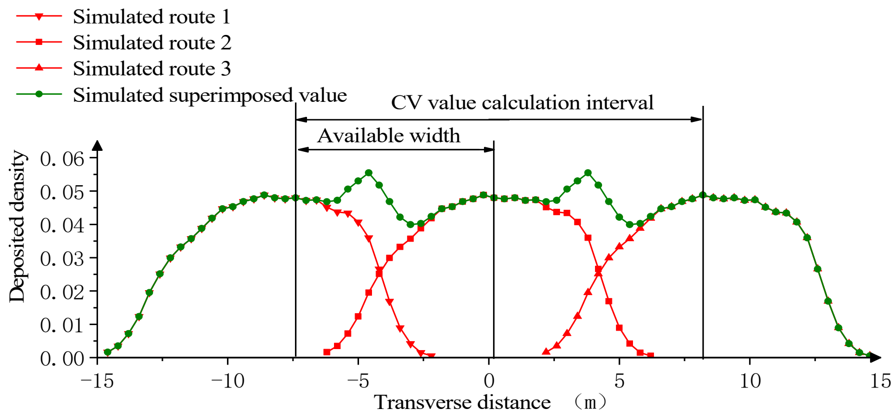

(**c**)

Figure 16. Simulation moving spread patterns. (**a**) Control group. (**b**) Honeycomb group. (**c**) Grid rectifier group.

4. Conclusions

To improve the uniformity of the MPGFS, the airflow field characteristics and motion trajectory of fertilizer particles were analyzed via CFD-DEM coupling simulation. The rotational airflow was supplied by a ducted fan, so that three vortices appeared in the shrinkage section. The tangential velocity of the rotational airflow in the middle approach was 10.03 m/s. Under the airflow, the trajectories of fertilizer particles were skewed. The simulation results showed that the rotational airflow was the main reason for the inconsistency of the discharge rate of each channel.

Two rectification methods concerning the use of the honeycomb rectifier and grid rectifier were developed. The rectification effects of the two rectifiers were analyzed using

CFD, and the key parameters were optimized. The CFD analysis results showed that the honeycomb aperture of 15 mm was better, and that the grid rectifier model of 5 × 10 was better. The maximum tangential velocity of the shrinkage section airflow with honeycomb and grid rectifiers was 4.73 m/s and 2.52 m/s, respectively. In contrast, the grid rectifier had a better rectification effect.

The discharge rate consistency test results of each channel showed that the consistency CV with honeycomb of aperture 15 mm was 13.07%, and with a grid rectifier model of 5 × 10 was 5.27%. Compared with the CV of 21.20% in the control group, the optimization schemes significantly improved the consistency discharge rate of each channel.

The optimized MPGFS was tested for spreading uniformity. The bench test results showed that there was a large number of depositional areas on the left side in the control group, and the spread pattern form was a single peak. After the honeycomb and grid rectifier, the spread patterns were a more reasonable circular arc. The CV of spreading uniformity in the control group was 15.32%, and that in the honeycomb group was 15.81%, and that in the grid rectifier group was 8.02%. After comprehensive analysis, the grid rectifier was selected as the final optimization scheme.

It was necessary to design the rectifier in the pneumatic spreader, especially the spreader powered by an axial flow fan. After rectification, the spreading uniformity of the MPGFS was improved, which provides a design reference for the spreader of variable rate fertilization UAV.

Author Contributions: Conceptualization, R.J., Z.Z., J.H. and J.L.; Methodology, X.W.; Software, X.W.; Validation, X.W., J.H. and J.L.; Formal analysis, X.W., R.J. and Z.Z.; Investigation, Z.Z.; Resources, R.J., Z.Z., J.H. and J.L.; Data curation, X.W.; Writing—original draft, X.W.; Writing—review & editing, X.W., R.J. and Z.Z.; Supervision, R.J., Z.Z., J.H. and J.L.; Project administration, R.J. and Z.Z.; Funding acquisition, Z.Z. All authors have read and agreed to the published version of the manuscript.

Funding: This work was supported by the Laboratory of Lingnan Modern Agriculture Project (Grant No. NT2021009); the Project of key R&D program of Guangzhou of China (Grant No. 202206010149), in part by Science and Technology Plan of Jian City of China (Grant No. 20211-055316 and [2020]83), Science and Technology Plan of Jian City of China (Grant No. 20211-055312), Science and Technology Plan of Guangdong Province of China (2023B10564002 and 2021B1212040009), Inno-vative Research Team of Agricultural and Rural Big Data in Guangdong Province of China (2019KJ138). The authors would like to thank the reviewers and editors for their constructive comments.

Data Availability Statement: The datasets used and/or analyzed during the current study are available from the corresponding author upon reasonable request.

Conflicts of Interest: The authors declare that they have no known competing financial interest or personal relationships that could have appeared to influence the work reported in this paper.

References

1. Jiang, R.; Sanchez-Azofeifa, A.; Laakso, K.; Wang, P.; Xu, Y.; Zhou, Z.; Luo, X.; Lan, Y.; Zhao, G.; Chen, X. UAV-based partially sampling system for rapid NDVI mapping in the evaluation of rice nitrogen use efficiency. *J. Clean. Prod.* **2021**, *289*, 125705. [CrossRef]
2. Kharim, M.N.A.; Wayayok, A.; Mohamed Shariff, A.R.; Abdullah, A.F.; Husin, E.M. Droplet deposition density of organic liquid fertilizer at low altitude UAV aerial spraying in rice cultivation. *Comput. Electron. Agric.* **2019**, *167*, 105045. [CrossRef]
3. Zhan, Y.; Chen, P.; Xu, W.; Chen, S.; Han, Y.; Lan, Y.; Wang, G. Influence of the downwash airflow distribution characteristics of a plant protection UAV on spray deposit distribution. *Biosyst. Eng.* **2022**, *216*, 32–45. [CrossRef]
4. Liu, W.; Zhou, Z.; Xu, X.; Gu, Q.; Zou, S.; He, W.; Luo, X.; Huang, J.; Lin, J.; Jiang, R. Evaluation method of rowing performance and its optimization for UAV-based shot seeding device on rice sowing. *Comput. Electron. Agric.* **2023**, *207*, 107718. [CrossRef]
5. Zhou, H.; Wang, X.; Au, W.; Kang, H.; Chen, C. Intelligent robots for fruit harvesting: Recent developments and future challenges. *Precis. Agric.* **2022**, *23*, 1856–1907. [CrossRef]
6. Kang, H.; Wang, X.; Chen, C. Accurate fruit localisation using high resolution LiDAR-camera fusion and instance segmentation. *Comput. Electron. Agric.* **2022**, *203*, 107450. [CrossRef]
7. Hassler, S.C.; Baysal-Gurel, F. Unmanned Aircraft System (UAS) Technology and Applications in Agriculture. *Agronomy* **2019**, *9*, 618. [CrossRef]

8. Zhang, C.; Kovacs, J.M. The application of small unmanned aerial systems for precision agriculture: A review. *Precis. Agric.* **2012**, *13*, 693–712. [CrossRef]
9. Li, J.; Lan, Y.; Zhou, Z.; Zeng, S.; Huang, C.; Yao, W.; Zhang, Y.; Zhu, Q. Design and test of operation parameters for rice air broadcasting by unmanned aerial vehicle. *Int. J. Agric. Biol. Eng.* **2016**, *9*, 24–32.
10. Wu, Z.; Li, M.; Lei, X.; Wu, Z.; Jiang, C.; Zhou, L.; Ma, R.; Chen, Y. Simulation and parameter optimisation of a centrifugal rice seeding spreader for a UAV. *Biosyst. Eng.* **2020**, *192*, 275–293. [CrossRef]
11. Gao, X.; You, Z.; Wu, H.; Peng, B.; Wang, S.; Cao, M. Design and Experiment of Green Manure Seed Broadcast Sowing Device Based on Unmanned Aerial Vehicle Platform. *Trans. Chin. Soc. Agric. Mach.* **2022**, *53*, 76–85.
12. Ren, W.; Wu, Z.; Li, M.; Lei, X.; Zhu, S.; Chen, Y. Design and Experiment of UAV Fertilization Spreader System for Rice. *Trans. Chin. Soc. Agric. Mach.* **2021**, *52*, 88–98.
13. Späti, K.; Huber, R.; Finger, R. Benefits of Increasing Information Accuracy in Variable Rate Technologies. *Ecol. Econ.* **2021**, *185*, 107047. [CrossRef]
14. Basso, B.; Dumont, B.; Cammarano, D.; Pezzuolo, A.; Marinello, F.; Sartori, L. Environmental and economic benefits of variable rate nitrogen fertilization in a nitrate vulnerable zone. *Sci. Total Environ.* **2016**, *545–546*, 227–235. [CrossRef]
15. Shi, Y.; Chen, M.; Wang, X.; Odhiambo, M.O.; Ding, W. Numerical simulation of spreading performance and distribution pattern of centrifugal variable-rate fertilizer applicator based on DEM software. *Comput. Electron. Agric.* **2018**, *144*, 249–259.
16. Song, C.; Zhou, Z.; Jiang, R.; Luo, X.; He, X.; Ming, R. Design and parameter optimization of pneumatic rice sowing device for unmanned aerial vehicle. *Trans. Chin. Soc. Agric. Eng.* **2018**, *34*, 80–88.
17. Song, C.; Zhou, Z.; Zang, Y.; Zhao, L.; Yang, W.; Luo, X.; Jiang, R.; Ming, R.; Zang, Y.; Zi, L.; et al. Variable-rate control system for UAV-based granular fertilizer spreader. *Comput. Electron. Agric.* **2021**, *180*, 105832. [CrossRef]
18. Song, C.; Zang, Y.; Zhou, Z.; Luo, X.; Zhao, L.; Ming, R.; Zi, L.; Zang, Y. Test and Comprehensive Evaluation for the Performance of UAV-Based Fertilizer Spreaders. *IEEE Access* **2020**, *8*, 202153–202163. [CrossRef]
19. Gao, X.; Zhou, Z.; Xu, Y.; Yu, Y.; Su, Y.; Cui, T. Numerical simulation of particle motion characteristics in quantitative seed feeding system. *Powder Technol.* **2020**, *367*, 643–658. [CrossRef]
20. Lei, X.; Liao, Y.; Liao, Q. Simulation of seed motion in seed feeding device with DEM-CFD coupling approach for rapeseed and wheat. *Comput. Electron. Agric.* **2016**, *131*, 29–39. [CrossRef]
21. Li, Y.; Liu, R.; Liu, C.; Liu, L. Test of Seed Velocity of Seed Tube Based on EDEM-Fluent Coupling. *Trans. Chin. Soc. Agric. Mach.* **2021**, *52*, 54–61.
22. Zang, Y.; Hou, X.; Wang, P.; Zhou, Z.; Jiang, R.; Li, K. A Study on Huanghuazhan Rice Fertilization Decision Model Based on Remote Sensing Technology of Unmanned Aerial Vehicle. *J. Shenyang Agric. Univ.* **2019**, *50*, 324–330.
23. Zhang, J.; Liu, G. Effects of control sequence optimisation on the performance of bivariate fertiliser applicator. *Comput. Electron. Agric.* **2022**, *192*, 106594. [CrossRef]
24. Su, N.; Xu, T.; Song, L.; Wang, R.; Wei, Y. Variable rate fertilization system with adjustable active feed-roll length. *International J. Agric. Biol. Eng.* **2015**, *8*, 19–26.
25. Song, C.; Zhou, Z.; Wang, G.; Wang, X.; Zang, Y. Optimization of the groove wheel structural parameters of UAV-based fertilizer apparatus. *Trans. Chin. Soc. Agric. Eng.* **2021**, *37*, 1–10.
26. Sun, J.; Chen, H.; Duan, J.; Liu, Z.; Zhu, Q. Mechanical properties of the grooved-wheel drilling particles under multivariate interaction influenced based on 3D printing and EDEM simulation. *Comput. Electron. Agric.* **2020**, *172*, 105329. [CrossRef]
27. Ai, J.; Chen, J.; Rotter, J.M.; Ooi, J.Y. Assessment of rolling resistance models in discrete element simulations. *Powder Technol.* **2011**, *206*, 269–282. [CrossRef]
28. Cool, S.; Pieters, J.; Mertens, K.C.; Hijazi, B.; Vangeyte, J. A simulation of the influence of spinning on the ballistic flight of spherical fertiliser grains. *Comput. Electron. Agric.* **2014**, *105*, 121–131. [CrossRef]
29. Laín, S.; Sommerfeld, M. Numerical calculation of pneumatic conveying in horizontal channels and pipes: Detailed analysis of conveying behaviour. *Int. J. Multiph. Flow* **2012**, *39*, 105–120. [CrossRef]
30. Kuang, S.; Zhou, M.; Yu, A. CFD-DEM modelling and simulation of pneumatic conveying: A review. *Powder Technol.* **2020**, *365*, 186–207. [CrossRef]
31. Deng, Y.; Mi, B.; Zhang, Y. Research on Numerical Calculation for Aerodynamic Characteristics Analysis of Ducted Fan. *J. Northwest. Polytech. Univ.* **2018**, *36*, 1045–1051. [CrossRef]
32. Ye, X.; Ding, X.; Zhang, J.; Li, C. Numerical simulation of pressure pulsation and transient flow field in an axial flow fan. *Energy* **2017**, *129*, 185–200. [CrossRef]
33. Li, C.; Lin, Q.; Ding, X.; Ye, X. Performance, aeroacoustics and feature extraction of an axial flow fan with abnormal blade angle. *Energy* **2016**, *103*, 322–339. [CrossRef]
34. Liu, J.; Gao, C.; Nie, Y.; Yang, B.; Ge, R.; Xu, Z. Numerical simulation of Fertilizer Shunt-Plate with uniformity based on EDEM software. *Comput. Electron. Agric.* **2020**, *178*, 105737. [CrossRef]
35. Zhu, Q.; Wu, G.; Chen, L.; Zhao, C.; Meng, Z. Influences of structure parameters of straight flute wheel on fertilizing performance of fertilizer apparatus. *Trans. Chin. Soc. Agric. Eng.* **2018**, *34*, 12–20.
36. Liu, C.; Li, Y.; Song, J.; Ma, T.; Wang, M.; Wang, X.; Zhang, C. Performance analysis and experiment on fertilizer spreader with centrifugal swing disk based on EDEM. *Trans. Chin. Soc. Agric. Eng.* **2017**, *33*, 32–39.

37. Wen, X.; Yuan, H.; Wang, G.; Jia, H. Calibration Method of Friction Coefficient of Granular Fertilizer by Discrete Element Simulation. *Trans. Chin. Soc. Agric. Mach.* **2020**, *51*, 115–122.
38. Coetzee, C.J.; Lombard, S.G. Discrete element method modelling of a centrifugal fertiliser spreader. *Biosyst. Eng.* **2011**, *109*, 308–325. [CrossRef]
39. ASAE (Ed.) Calibration and Distribution Pattern Testing of Agricultural Aerial Application Equipment. In *ASAE S386.2*; ASAE: Washington, DC, USA, 2013.